Multi-view Self-supervised Disentanglement for General Image Denoising

Hao Chen[*,1] Chenyuan Qu[*,1] Yu Zhang[2] Chen Chen[3] Jianbo Jiao[1]

[1]University of Birmingham [2]Shanghai Jiao Tong University [3]University of Central Florida

Project page: https://chqwer2.github.io/MeD/

Abstract

*With its significant performance improvements, the deep learning paradigm has become a standard tool for modern image denoisers. While promising performance has been shown on seen noise distributions, existing approaches often suffer from generalisation to unseen noise types or general and real noise. It is understandable as the model is designed to learn paired mapping (e.g. from a noisy image to its clean version). In this paper, we instead propose to learn to disentangle the noisy image, under the intuitive assumption that different corrupted versions of the same clean image share a common latent space. A self-supervised learning framework is proposed to achieve the goal, without looking at the latent clean image. By taking two different corrupted versions of the same image as input, the proposed **M**ulti-view **S**elf-supervised **D**isentanglement (MeD) approach learns to disentangle the latent clean features from the corruptions and recover the clean image consequently. Extensive experimental analysis on both synthetic and real noise shows the superiority of the proposed method over prior self-supervised approaches, especially on unseen novel noise types. On real noise, the proposed method even outperforms its supervised counterparts by over **3 dB**.*

1. Introduction

Image restoration is a critical sub-field of computer vision, exploring the reconstruction of image signals from corrupted observations. Examples of such ill-posed low-level image restoration problems include image denoising [16, 25, 26, 29, 33, 35, 38], super-resolution [2, 8, 19, 30, 37], and JPEG artefact removal [7, 12, 31], to name a few. Usually, a mapping function dedicated to the training data distribution is learned between the corrupted and clean images to address the problem. While many image restoration systems perform well when evaluated over the same corruption distribution that they have seen, they are often required to be deployed in settings where the environment is unknown and
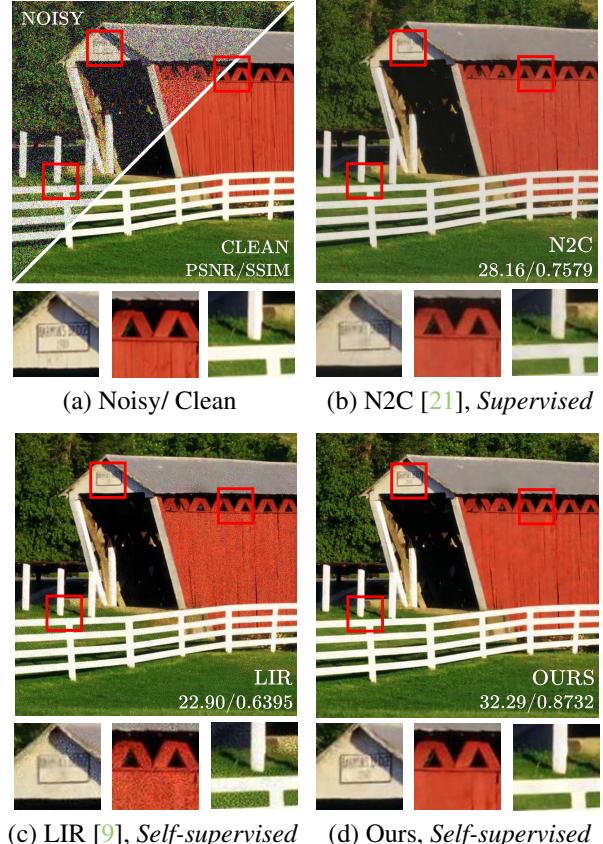

Figure 1. **Denoising performance on unseen Speckle Noise with $\hat{v} = 50$.** The models were trained with Gaussian noise $\sigma \in [5, 50]$. (a) The noisy and clean images, with ground-truth clean patches shown below. (b) *Noise-to-Clean (N2C)* [21] is trained with clean images. (c) *LIR* [9] is self-supervised but needs unpaired clean images as training data. (d) Our approach is fully self-supervised, training with only the noisy input data.

off the training distribution. These settings, such as medical imaging, computational lithography, and remote sensing, require image restoration methods that can handle complex and unknown corruptions. Moreover, in many real-world image-denoising tasks, ground truth images are unavailable, introducing additional challenges.

---

[*]Equal contribution.

Limitations of existing methods: Current low-level corruption removal tasks aim to address the inquiry of "what is the clean image provided a corrupted observation?" However, the ill-posed nature of this problem formulation poses a significant challenge in obtaining a unique resolution [5].

To mitigate this limitation, researchers often introduce additional information, either explicitly or implicitly. For example, in [15], *Laine et al.* explicitly use the prior knowledge of noise as complementary input, generating a new invertible image model. Alternatively, Learning Invariant Representation (LIR) [9] implicitly enforces the interpretability in the feature space to guarantee the admissibility of the output. However, these additional forms of information may not always be practical in real-world scenarios or may not result in satisfactory performance.

Main idea and problem formulation: Our motivation for tackling this ill-posed nature stems from the solution in the 3D reconstruction of utilising multiple views to provide a unique estimation of the real scene [1]. Building on this motivation, we propose a training scheme that is explicitly built on multi-corrupted views and perform **M**ulti-view s**e**lf-supervised **D**isentanglement, abbreviated as *MeD*.

Under this new multi-view setting, we reformulate the task problem as **"what is the shared latent information across these views?"** instead of the conventional "what is the clean image?" By doing so, MeD can effectively leverage the scene coherence of multi-view data and capture underlying common parts without requiring access to the clean image. This makes it more practical and scalable in real-world scenarios. An example of the proposed method with comparison to prior works is shown in Figure 1, indicating its effectiveness over the state-of-the-art.

Specifically, given any scene image $x^k \sim \mathcal{X}, k \in \mathbb{N}$ sampled uniformly from a clean image set $\mathcal{X}$, MeD produces two contaminated views:

$$y_1^k \triangleq \mathcal{T}_1(x^k), \; y_2^k \triangleq \mathcal{T}_2(x^k), \tag{1}$$

forming two independent corrupted image sets $\{\mathcal{Y}_1\}, \{\mathcal{Y}_2\}$, where $y_1^k \in \mathcal{Y}_1, y_2^k \in \mathcal{Y}_2$. The $\mathcal{T}_1$ and $\mathcal{T}_2$ represent two random independent image degradation operations.

We parameterise our scene feature encoder $G_\theta^\mathcal{X}$ and decoder $D_\psi^\mathcal{X}$ with θ and ψ. Considering the image pair $\{y_1^k, y_2^k\}_{k \in \mathbb{N}}$, the core of the presented method can be summarised as:

$$G_\theta^\mathcal{X}(y_1^k) \triangleq z_x^{k,i} \triangleq G_\theta^\mathcal{X}(y_2^k), \tag{2}$$

$$\hat{x}^k \triangleq D_\psi^\mathcal{X}(z_x^{k,i}), \tag{3}$$

where $z_x^{k,i}$ represents the shared scene latent between y_1^k and y_2^k with i referring to the input image index of y_i. A clean image estimator $D_\psi^\mathcal{X}$ forms an all-deterministic reverse mapping from $z_x^{k,i}$ to reconstruct an estimated clean image $\hat{x}^k$. Similarly, the noise latent $u_\eta^{k,i}$ is factorised from a corrupted view with a corruption encoder $E_\rho^\mathcal{N}$. Afterwords, the resulting corruption is reconstructed from $u_\eta^{k,i}$ through the use of a corruption decoder, represented by $F_\phi^\mathcal{N}$.

The *disentanglement* is then performed between $\{z_x^{k,i}, u_\eta^{k,j}\}_{i \neq j}$ on a cross compose decoder $R_\delta^\mathcal{Y}$ with parameter δ, which can be formulated as:

$$\hat{y}_1^k \triangleq R_\delta^\mathcal{Y}(z_x^{k,2}, u_\eta^{k,1}). \tag{4}$$
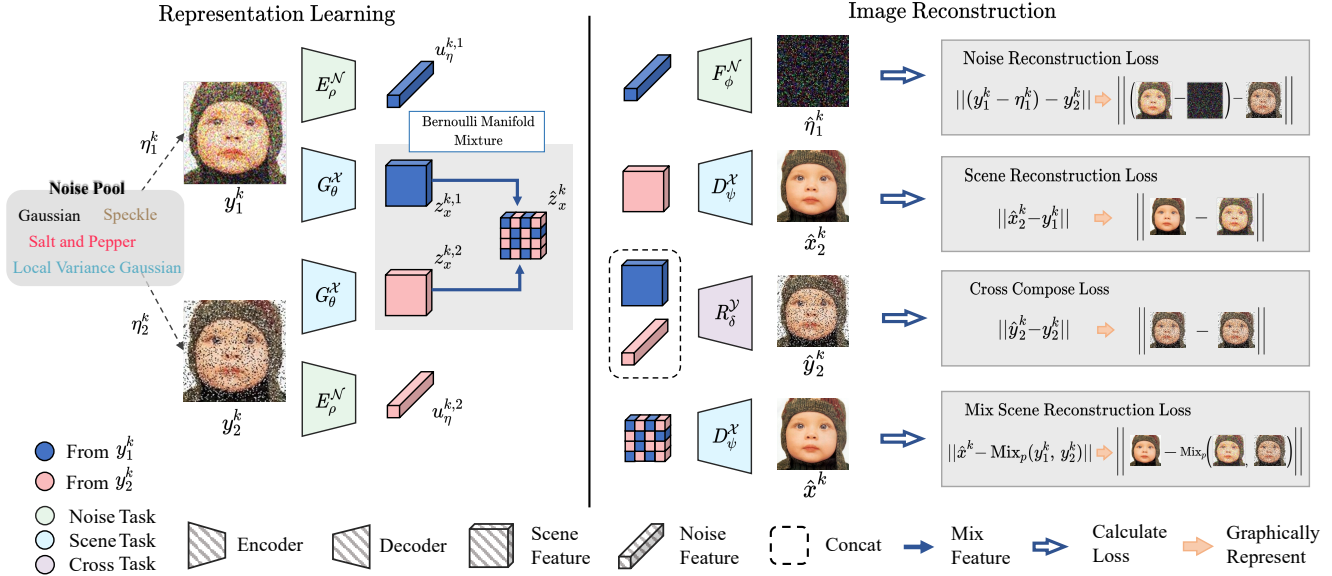
It should be noted that Equation (4) is performed over latent features u and z from different views. When assuming that z_x^k remains constant across views, the reconstructed view $\hat{y}_1^k$ is determined by the $u_\eta^{k,1}$.

Contributions. The contributions of our work are summarised as follows:

- We propose a new problem formulation to address the ill-posed problem of image denoising using only noisy examples, in a different paradigm than prior works.

- We introduce a disentangled representation learning framework that leverages multiple corrupted views to learn the shared scene latent, by exploiting the coherence across views of the same scene and separating noise and scene in the latent space.

- Extensive experimental analysis validates the effectiveness of the proposed *MeD*, outperforming existing methods with more robust performance to unknown noise distributions, even better than its supervised counterparts.

2. Related Work

Single-view image restoration: In [8], *Dong et al.* were the first to employ a deep network in super-resolution. Later, a range of single view-based models expanded the idea of supervised deep learning to handle image restoration tasks, such as deblurring [14], JPEG artefacts [12], inpainting [17, 34] and denoising [16, 26, 35]. Recently, it is receiving increasing interest in relaxing the prerequisite of supervised learning with corrupted/ clean image pairs. In the context of image denoising, the "*corrupted/clean*" pair denotes a corrupted input image and its corresponding clean image for calculating the loss. To tackle the issue of the lack of clean data, several methods have been proposed, such as the Noise2Noise (N2N) method [16] and Recorrupted-to-Recorrupted (R2R) [26], which train deep networks on pairs of noisy images. Noise2Void (N2V) [13], Noise2Self (N2S) [4], and the method proposed by *Laine et al.* [15] are based on the blind-spot strategy that discards some pixels in the input and predicts them using the remaining. In the field

Figure 2. **Method Overview.** This figure illustrates the main steps of our proposed method, MeD, which first generates *scene features* (cubes) and *distortion features* (cuboids). The colour of them indicates their image source. In the right section, the features are rearranged and utilised for the four forward paths, from top to bottom, which are the reconstructions of noise ($\hat{\eta}_1^k$), scene ($\hat{x}_2^k$), input image (y_2^k) and shared scene ($\hat{x}^k$). It is noteworthy that $\hat{y}_2^k$ is reconstructed using $z_x^{k,1}$ from y_1^k and $u_\eta^{k,2}$ from y_2^k for feature disentanglement. Additionally, the reconstruction of $\hat{x}^k$ relies on mixed scene features to facilitate learning of invariant scene latent. Moreover, the reconstruction paths for ($\hat{\eta}_2$, $\hat{x}_1$, and y_1) are not depicted here, as they differ from the given paths only in their sub-indexes.

of single-image denoising, some methods such as DIP [29] and S2S [27], have achieved remarkable denoising results using only one noisy image.

These methods, however, often inevitably compromise image quality to noise reduction, resulting in over-smoothed output. This trade-off is further exacerbated under domain shifts when dealing with unknown noise distributions.

Restoration based on multiple views: Existing multi-view variants of image restoration methods mainly focus on sequential data such as video or burst images. For example, *Tico* [28] builds a paradigm that separates the unique and common features within the multi-frame to produce a denoised estimate. *Liu et al.* [20] models degrading elements as foreground and estimate background using video data. Deep Burst Denoising (DBD) [11] performs multi-view denoising based on burst images. Each image is taken in a short exposure time and serves as a corrupted observation of the clean image.

Unlike the above-mentioned methods, our *MeD* aims to use multiple static observations simultaneously to learn the latent representation of a clean scene that is shared by multiple discrete views.

Self-supervised feature disentanglement: Another notable path of work has attempted to disentangle underlying invariant content from distorted images. For instance, *UID-*

GAN [22] utilises unpaired clean/blurred images to disentangle content and blurring effects in the feature space and yield improved deblurring performance. Similarly, *LIR* [9] used unpaired input to isolate invariant content features through self-supervised inter-domain transformation.

However, these methods are limited to synthetic noise and do not extend well in real-world scenarios due to their reliance on clean images. In contrast, our method is purely based on multiple noisy views of the same static scene and aims to disentangle the scene from corruption, without the need for clean image supervision.

3. Methodology

Our primary objective is to identify the commonalities among different views in the denoising process. To achieve this, we aim to discover the shared scene z_x^k that is degradation-agnostic over various corrupted views $\{y_i^k\}_{k\in\mathbb{N}}$ via our proposed training schema, namely ***M**ulti-view **s**elf-supervised **D**isentanglement* (MeD). A graphic depiction of MeD is shown in Figure 2, composed of the representation learning process in the left panel, and four distinct reconstruction pathways in the right panel.

The detailed design of the proposed schema will be introduced in the following subsections. Section 3.1 explains the restoration of noise and scene. Section 3.2 details the reconstruction of noisy input using a cross-feature combination. Section 3.3 elaborates on the reconstruction of the

scene using mixed scene latent.

We will start our introduction by outlining three essential properties that a multi-view representation disentanglement technique should exhibit.

Pre-assumed properties: Suppose the scene latent space and corruption latent space are symbolised by $\mathcal{Z}_x$ and $\mathcal{U}_\eta$, respectively.

(1) Independence: For any scene latent $z_x^k \in \mathcal{Z}_x$, it is expected to be independent of any corruption latent $u_\eta^{k,i}, \in \mathcal{U}_\eta$.

(2) Consistency: There exists one shared latent code $z_x^k \in \mathcal{Z}_x$ that is capable of representing the shared clean component of all instances in the set $\{y_i^k\}$.

(3) Composability: Recovery of the corrupted view y_i^k can be achieved using the feature pairs $z_x^k, u_\eta^{k,i}$, and the index of the recovered view is determined by the index of the corruption latent, which represents the unique component within that particular view.

A key step of our method is to realise these pre-requisitions by determining how to implement the latent space assumption. As shown in the left panel of Figure 2, to infer our latent space assumption, MeD is comprised of two encoders and three decoders: A shared content latent *encoder* $G_\theta^{\mathcal{X}}$ and its *decoder* $D_\psi^{\mathcal{X}}$, an auxiliary noise latent *encoder* $E_\rho^{\mathcal{N}}$ and its *decoder* $F_\phi^{\mathcal{N}}$, and a cross disentanglement *decoder* $R_\delta^{\mathcal{Y}}$.

3.1. Main Forward Process

Given two corrupted views of the same image x^k, $y_1^k \triangleq \mathcal{T}_1(x^k)$ and $y_2^k \triangleq \mathcal{T}_2(x^k)$, the *encoder* $G_\theta^{\mathcal{X}}$ mainly perform the scene feature space encoding that can be formulated as:

$$z_x^{k,1} \triangleq G_\theta^{\mathcal{X}}(y_1^k), \ z_x^{k,2} \triangleq G_\theta^{\mathcal{X}}(y_2^k), \tag{5}$$

where $z_x^{k,1}$ and $z_x^{k,2}$ are the estimation of the scene feature corresponding to the inputs y_1^k and y_2^k.

The process of clean image reconstruction is then completed by the $D_\psi^{\mathcal{X}}$:

$$\hat{x}_1^k \triangleq D_\psi^{\mathcal{X}}(z_x^{k,1}), \ \hat{x}_2^k \triangleq D_\psi^{\mathcal{X}}(z_x^{k,2}). \tag{6}$$

Similar to the process of estimating scene features, the estimation of distortion features by $E_\rho^{\mathcal{N}}$, followed by the reconstruction of noise with $F_\phi^{\mathcal{N}}$, can be described as follows:

$$
\begin{aligned}
u_n^{k,1} &\triangleq E_\rho^{\mathcal{N}}(y_1^k), \ u_n^{k,2} \triangleq E_\rho^{\mathcal{N}}(y_2^k), \\
\hat{\eta}_1^k &\triangleq F_\phi^{\mathcal{N}}(u_n^{k,1}), \ \hat{\eta}_2^k \triangleq F_\phi^{\mathcal{N}}(u_n^{k,2}).
\end{aligned}
\tag{7}
$$

We adhere to the methodology introduced by N2N [16] to use noisy images as supervisory signals. The objective function of the aforementioned process can be simplified to:

$$
\begin{aligned}
\underset{\theta,\psi}{\arg\min} \ \mathcal{L}^{\mathcal{X}} &\triangleq ||\hat{x}_1^k - y_2^k||, \\
\underset{\rho,\phi}{\arg\min} \ \mathcal{L}^{\mathcal{N}} &\triangleq ||(y_1^k - \hat{\eta}_1^k) - y_2^k||.
\end{aligned}
\tag{8}
$$

The objective of $\hat{x}_2^k$ and $\hat{\eta}_2^k$ are the same as above, with only a subscript difference. It should be noted that, although our objective functions are similar to that of N2N, our goal is not simply to find and remove noise, but rather to capture the common features shared across multiple views.

3.2. Cross Disentanglement

For general latent codes z_x^k to sufficiently represent scene information in the image space, it is natural to assume that these codes exhibit a certain degree of freedom, allowing them to intersect with the noise space. Consequently, there is no guarantee of complete isolation between z_x^k and u_η^k. To meet the requirements of properties (1) and (3), we use an additional decoder $R_\delta^{\mathcal{Y}}$ to reconstruct a corrupted view over a cross-feature combination, e.g. $z_x^{k,1}$ from y_1 and $u_n^{k,2}$ from x_2, which can be represented as:

$$\hat{y}_1^k \triangleq R_\delta^{\mathcal{Y}}(z_x^{k,2}, u_n^{k,1}), \ \hat{y}_2^k \triangleq R_\delta^{\mathcal{Y}}(z_x^{k,1}, u_n^{k,2}). \tag{9}$$

This realisation explicitly requires $z_x^{k,i}$ to represent the common part and $u_n^{k,j}$ to represent the unique part within the corrupted views. We then optimise $\{\theta, \rho, \delta\}$ from $\{G_\theta^{\mathcal{X}}, E_\rho^{\mathcal{N}}, R_\delta^{\mathcal{Y}}\}$ using the following objective:

$$\underset{\theta,\rho,\delta}{\arg\min} \ \mathcal{L}^{\mathcal{C}} \triangleq ||\hat{y}_1^k - y_1^k|| + ||\hat{y}_2^k - y_2^k||. \tag{10}$$

Generally, it is possible for there to be a trivial solution from $u_n^{k,i}$ to y_i^k in Equation (9) such as, when $u_n^{k,1}$ is extracted from y_1^k and used to reconstruct it as well. However, Equation (7) explicitly requires $u_n^{k,1}$ to rebuild the noise, which prevents the collapse of $u_n^{k,1}$ in expressing y_1^k.

3.3. Bernoulli Manifold Mixture

The aforementioned latent constraint might appear to be restricted at first, but in fact, it enables us to capture a large number of degrees of freedom in latent space implementation. For instance, it is possible to have multiple scene features that correspond to a single scene. However, in such cases, the mapping from input to scene features becomes ambiguous. To tackle this issue, we propose the use of the *Bernoulli Manifold Mixture* (BMM) as a means of leveraging the shared structure within the scene latent.

Given the assumption of property (2), the acquired scene features $z_x^{k,1}$ and $z_x^{k,2}$ are expected to be identical and interchangeable with one another, as they both refer to the same scene feature. BMM establishes a new explicit connection

between the scene features of multi-views, which can be expressed in the equation as:

$$\hat{z}_x^k \triangleq \text{Mix}_p(z_x^{k,1}, z_x^{k,2}), \tag{11}$$

where the $\hat{z}_x^k$ is an estimation of the true underlying scene feature. Let b_f define a sample instance drawn from a Bernoulli distribution with probability $p \in (0, 1)$, the function $\text{Mix}_p(\cdot)$ described in Equation (11) denotes:

$$\text{Mix}_p(\boldsymbol{m}, \boldsymbol{n}) \triangleq b_f \odot \boldsymbol{m} + (1 - b_f) \odot \boldsymbol{n}. \tag{12}$$

By establishing this new connection (Equation 11), we can enhance the interchangeability between $z_x^{k,1}$ and $z_x^{k,2}$ by optimising the reconstruction performance on $\hat{z}_x^k$.

Lemma 1. *Assuming $z_x^{k,i} \sim N_{\mathbf{x}}(\boldsymbol{\mu}, \boldsymbol{\Sigma})$, where $N_{\mathbf{x}}$ denotes multivariate Gaussian distributions and then $\boldsymbol{\mu}$ and $\boldsymbol{\Sigma}$ is the mean and the covariance matrix.*

For a given function $G_\theta^{\mathcal{X}}(\cdot)$, assume $\forall k, i, m, n \in \mathbb{N}$, the following property holds:

$$\mathbb{E}\left[G_\theta^{\mathcal{X}}(z_x^{k,i})\right] \triangleq \mathbb{E}\left[G_\theta^{\mathcal{X}}(\text{Mix}_p(z_x^{k,m}, z_x^{k,n}))\right]. \tag{13}$$

Proof. Assume $z_x^{k,m}, z_x^{k,n} \in \mathbb{R}^{\dim}$ are i.i.d., we may also factorise $b_f \in \mathbb{R}^{\dim}$. Write

$$\hat{z}_x^k \triangleq \text{Mix}_p(z_x^{k,m}, z_x^{k,n}) \tag{14}$$

so that we can have

$$\begin{aligned}\hat{z}_x &\sim N_{\mathbf{x}}((b_f + 1 - b_f)\boldsymbol{\mu}, (b_f^2 + (1 - b_f)^2)\boldsymbol{\Sigma}) \\ &\sim N_{\mathbf{x}}(\boldsymbol{\mu}, \boldsymbol{\Sigma})\end{aligned} \tag{15}$$

with the fact that Bernoulli sample $b_f^2 = b_f$, the mixed feature $\hat{z}_x$ is in the same representation distribution as $z_x^{k,i}$.

In MeD, we denote $\hat{z}_x = G_\theta^{\mathcal{X}}(\hat{z}_x^k)$, and the objective for implementing Equation (13) can be formulated as follows:

$$\underset{\theta, \rho, \psi}{\arg\min} \mathcal{L}^{\mathcal{M}} \triangleq \lambda \|\hat{z}_x - \text{Mix}_p(y_1^k, y_2^k)\|, \tag{16}$$

where the λ is the weight parameter. Here, the target is using a mixed version of y_1^k and y_2^k. The choice of this is driven by the intuition that the hybrid version would better align with the aforementioned blended features.

4. Experiments

To evaluate the effectiveness of our proposed method, we assess our method against several representative self-supervised denoising methods, including Noise2Noise (N2N) [16], Noise2Self (N2S) [4] and Recorrupted2Recorrupted (R2R) [26], and the invariant feature learning method LIR [9]. Moreover, we also evaluate our approach against two supervised baseline methods (Noise2Clean (N2C) [21] and multi-frame method DBD [11]) to further validate its effectiveness. Comparisons to more methods, including methods using only one noisy image, are presented in the supplementary material.

We start our experiments by denoising synthetic additive white Gaussian noise (AWGN) in Section 4.2, and then move on to testing unseen noise levels and noise types in Section 4.3 and Section 4.4, respectively. Furthermore, we evaluate the performance in real-world scenarios in Section 4.5. In Section 4.6, we expand our experiments to incorporate more views to study their impact on performance. Finally, in Section 4.7, we apply our method to other tasks, *e.g.* image super-resolution and inpainting, to demonstrate its generalisation ability.

4.1. Experimental Setups

Noted that, the nature of feature disentanglement requires no leak from input to output, however, the global residual connection of the original DnCNN [35] cannot satisfy. Thus, we incorporate the *Swin-Transformer* (Swin-T) [21] instead of the traditionally used DnCNN in our experiments. Nevertheless, as Swin-T is not originally designed for image restoration, we make some modifications to enforce local dependence across the image. Specifically, we add one Convolution Layer each before the patch embedding and after the patch unembedding of Swin-T, as inspired by SwinIR [18]. The resulting modified network backbone is denoted as *Swin-Tx*.

To ensure a fair comparison, we use the *Swin-Tx* backbone for all methods in our study, except for DBD. As DBD did not release the code, we follow the instructions presented in the paper and make our best effort to re-implement it. However, we observe that the two-view DBD could not converge efficiently, which is consistent with the findings in the paper. Therefore, we limit our evaluation to the four-view DBD, denoted as DBD_4. Furthermore, we replace the U-Net backbone originally used in the LIR method with Swin-Tx to maintain consistency in our evaluation. This results in an average improvement of approximately 1 dB in PSNR for Gaussian denoising.

In all experiments, all methods were trained using only DIV2K [3] and the same optimisation parameters, except for LIR and DBD_4 which used manually selected parameters obtained through experiments. For more training and evaluation details including the choice of parameters, please refer to the supplementary material. Code is available at: https://github.com/chqwer2/Multi-view-Self-supervised-Disentanglement-Denoising.

Remark: In tables, the best results are highlighted in **bold**, while the second best is underlined.

Table 1. Quantitative comparison of different methods on CBSD68 Dataset [23] for Synthetic Gaussian noise. The experiments were conducted on fixed and random variance, respectively. The best results are highlighted in **bold**, while the second best is <u>underlined</u>.

Training Schema	Test $\hat{\sigma}$	Noisy/ Clean		Noisy/ Noisy			Invariant Feature	
		N2C [21]	DBD$_4$ [11]	N2N [16]	N2S [4]	R2R [26]	LIR [9]	MeD (ours)
Gaussian $\sigma = 25$	15	<u>33.36/ 0.9020</u>	**33.57/ 0.9092**	32.64/ 0.8805	32.77/ 0.8780	29.74/0.7865	31.06/ 0.8632	33.11/ 0.8880
	25	30.83/ 0.8494	**31.31/ 0.8548**	30.68/ 0.8334	<u>30.99/ 0.8405</u>	30.45/0.8183	30.01/ 0.8024	30.57/ <u>0.8496</u>
	50	24.76/ 0.5519	<u>25.12/ 0.5583</u>	24.59/ 0.5385	22.13/ 0.3928	24.02/0.5133	21.97/ 0.3578	**25.67/ 0.6026**
	75	20.75/ 0.3376	<u>21.09/ 0.3412</u>	20.60/ 0.3162	17.86/ 0.1998	19.10/0.2641	16.23/ 0.1689	**23.09/ 0.4320**
Gaussian $\sigma \in [5, 50]$	15	<u>33.47/ 0.9027</u>	33.12/ 0.8915	33.45/ 0.8945	31.28/ 0.8187	20.76/ 0.2508	30.85/ 0.8431	**33.62/ 0.9026**
	25	<u>30.87/ 0.8538</u>	30.64/ 0.8491	30.77/ 0.8423	29.65/ 0.7801	23.91/ 0.4552	28.92/ 0.8069	**30.91/ 0.8573**
	50	<u>27.41/ 0.7361</u>	27.13/ 0.7290	27.15/ 0.7219	27.00/ 0.7114	26.92/ 0.6911	25.13/ 0.6191	**27.48/ 0.7530**
	75	<u>25.05/ 0.6223</u>	24.97/ 0.6205	24.80/ 0.5908	24.89/ 0.6023	23.83/ 0.5132	22.37/ 0.4212	**25.40/ 0.6645**

Table 2. Quantitative result of generalisation performance experiment on CBSD68 [23]. All methods use Gaussian $\sigma = 25$ for pre-trained methods and then Gaussian $\sigma \in [5, 50]$ for fine-turning. The better result in each method is highlighted in *italics*.

Fine-tuning Method Pretraining Method	N2C [21]		N2N [16]		LIR [9]		MeD
	N2C	MeD	N2N	MeD	LIR	MeD	MeD
Gaussian, $\hat{\sigma} \in [15, 75]$	29.20/ 0.7797	*29.53/ 0.8081*	29.04/ 0.7642	*29.21/ 0.7890*	26.42/ 0.6640	*27.25/ 0.7036*	**29.60/ 0.8101**
Local Var Gaussian	35.62/ 0.9308	*35.85/ 0.9439*	35.66/ 0.9256	*35.73/ 0.9310*	29.26/ 0.8170	*30.51/ 0.8387*	**35.91/ 0.9762**
Poisson Noise	40.49/ 0.9736	*42.80/ 0.9776*	41.35/ 0.9736	*42.27/ 0.9813*	31.23/ 0.8672	*33.47/ 0.8932*	**45.05/ 0.9826**
Speckle, $\hat{v} \in [25, 50]$	33.36/ 0.9004	*33.40/ 0.9044*	33.32/ 0.8931	*33.33/* 0.8907	28.28/ 0.7713	*29.82/ 0.8229*	**33.48/ 0.9115**
S&P, $\hat{r} \in [0.3, 0.5]$	28.85/ 0.8267	*30.73/ 0.8372*	28.59/ 0.8003	*29.45/ 0.8255*	26.69/ 0.7241	*27.62/ 0.7460*	**30.84/ 0.9135**
Average	33.50/ 0.8822	*34.46/ 0.8942*	33.59/ 0.8714	*34.00/ 0.8835*	28.38/ 0.7687	*29.73/ 0.8009*	**34.98/ 0.9188**

4.2. AWGN Noise Removal

We first investigate the denoising generalisation of the methods using synthetic zero-mean additive white Gaussian noise (AWGN). The experiments are divided into two parts. The first segment employs fixed variance AWGN, whereas the second segment employs varied variance Gaussian for training in a separate manner. Table 1 summarises the quantitative results evaluated on CBSD68 Dataset [23] at variance levels of 15, 25, 50, and 75.

Analysis: In the fixed variance setting, MeD performs inferior compared to the other methods on lower noise levels of 15 and 25. However, as the methods face more severe corruption, MeD outperforms all self-supervised and supervised methods, showing our greater advantage of handling severe noise. For instance, at $\sigma = 75$, MeD outperforms the second-best method (N2C) by around 2 dB. These results suggest that MeD has a remarkable ability to generalise to a range of unseen noise levels in Gaussian noise.

In the context of random variance, it has been observed that MeD exhibits superior performance across all four noise levels compared to other methods, including supervised methods. These findings imply that MeD can benefit more from varying training noise than other methods. More experiments and details on AWGN noise removal can be found in the supplementary material.

4.3. Generalisation on Unseen Noise Removal

In the previous subsection, we demonstrated the remarkable generalisation ability of our model in the case of Gaussian noise. Here, we aim to extend this investigation to other types of unseen noise and evaluate the denoising generalisation ability of our method. Specifically, we consider Poisson noise, Speckle noise, Local Variance Gaussian noise, and Salt-and-Pepper noise. For a more detailed synthetic process, please refer to the supplementary material.

First, we demonstrate qualitative comparisons of denoising unseen noise types using models trained only with Gaussian $\sigma = 25$ in Figure 3. Next, in order to further verify the denoising generalisation ability of MeD, we employ its scene encoder and decoder as pre-trained models to be compared against other methods. It should be noted that the pre-training and fine-tuning methods employed in this study may differ, as shown in Table 2. The pre-training of all test models was conducted on a Gaussian sigma value of 25, followed by fine-tuning with a Gaussian sigma range of 5 to 50. Since the training schema of N2S, R2R, and DBD$_4$ differs from MeD, we do not include them in this section. However, evaluations of these methods on unseen noise are still presented in Section 4.4 under different settings.

Analysis: Qualitative results in Figure 3 show that under Gaussian $\sigma = 25$ training settings, our method surpasses other methods in denoising unseen noise types. Additionally, Table 2 shows that the approaches using pre-trained MeD models outperform their self-transfer models for N2C, N2N, and LIR, with improvements of up to 2 dB in some cases. On average, the MeD pre-trained models show a performance gain of around 0.5 dB across all methods, highlighting the potential of MeD as a powerful pre-training
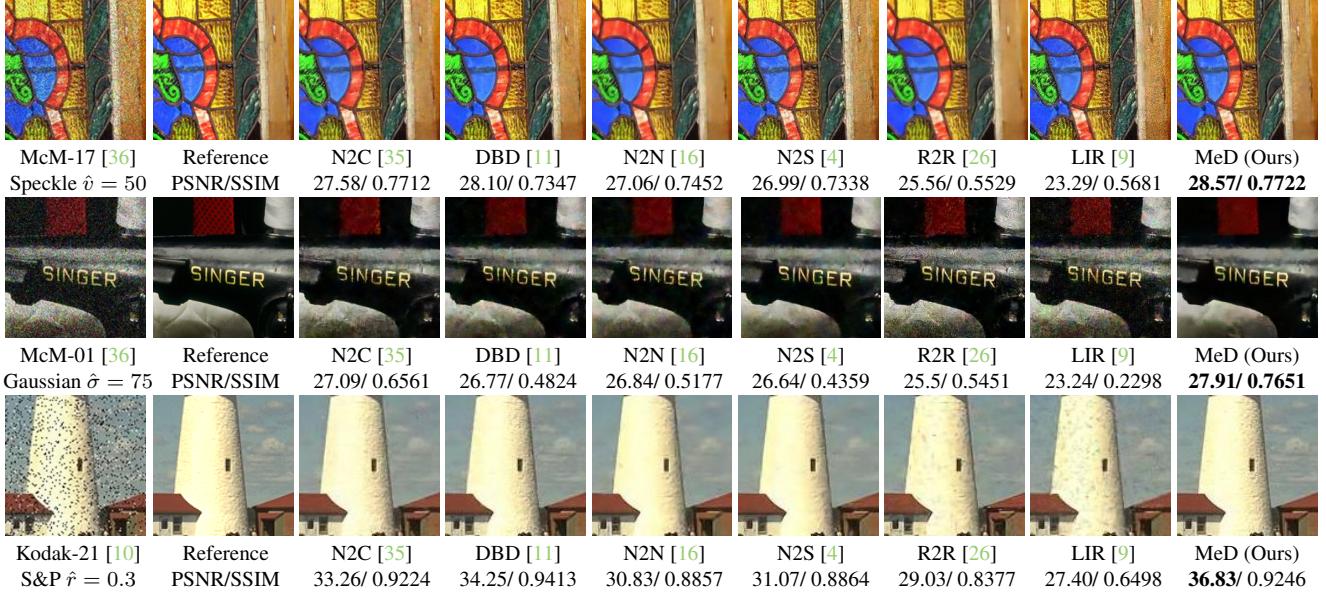
Figure 3. Qualitative denoising results on unseen noise types. All the methods are trained with Gaussian $\sigma = 25$. The quantitative PSNR/SSIM results are provided underneath the respective images. Best viewed in colour (zoom-in for a better comparison).

Table 3. Analysis of *Noise Pool* on CBSD68 [23]. All methods were trained using randomly drawn noise from the Noise Pool.

Test Noise	Noisy/ Clean		Noisy/ Noisy			Invariant Feature	
	N2C [21]	DBD$_4$ [11]	N2N [16]	N2S [4]	R2R [26]	LIR [9]	MeD (ours)
Gaussian, $\hat{\sigma} \in [15, 75]$	29.24/ 0.7754	29.05/ 0.7616	29.23/ 0.7634	28.58/ 0.7589	26.43/ 0.6639	26.67/ 0.6866	**29.61/ 0.8178**
Local Var Gaussian (LVG)	36.64/ 0.9442	36.18/ 0.9307	36.65/ 0.9235	33.24/ 0.8858	34.70/ 0.8779	31.61/ 0.8627	**37.99/ 0.9568**
Poisson Noise	45.72/ 0.9764	44.23/ 0.9606	45.64/ 0.9799	46.31/ 0.9808	44.45/ 0.9491	43.27/ 0.9292	**48.10/ 0.9916**
Speckle, $\hat{v} \in [25, 50]$	35.58/ 0.9417	35.24/ 0.9385	35.34/ 0.9475	35.13/ 0.9596	34.20/ 0.9078	33.98/ 0.8810	**37.21/ 0.9715**
S&P, $\hat{r} \in [0.3, 0.5]$	38.85/ 0.9165	37.10/ 0.8884	38.89/ 0.9289	38.22/ 0.9330	36.17/ 0.9087	33.43/ 0.8202	**42.33/ 0.9695**
Gaussian $\hat{\sigma} = 25$ + Speckle $\hat{v} = 25$	30.19/ 0.8279	29.24/ 0.8156	30.32/ 0.8317	29.51/ 0.8050	28.78/ 0.7744	29.20/ 0.7871	**31.92/ 0.8726**
Gaussian $\hat{\sigma} = 50$ + Speckle $\hat{v} = 25$	27.30/ 0.7251	26.55/ 0.7126	27.23/ 0.7331	26.91/ 0.7081	26.49/ 0.6935	26.19/ 0.6941	**29.68/ 0.7928**
LVG + Poisson	31.78/ 0.9087	31.10/ 0.8842	31.60/ 0.7617	30.15/ 0.8086	28.52/ 0.7144	27.33/ 0.7234	**34.29/ 0.9325**
Poisson + Speckle $\hat{v} = 25$	31.39/ 0.9069	30.86/ 0.8782	31.52/ 0.8935	30.58/ 0.9067	30.34/ 0.8897	29.93/ 0.8554	**33.04/ 0.9258**
Average	34.08/ 0.8803	33.28/ 0.8634	34.05/ 0.8626	33.18/ 0.8607	32.23/ 0.8199	31.29/ 0.8044	**36.02/ 0.9145**

method for image denoising. It is noteworthy that the self-transfer MeD model exhibits the best denoising performance across all validation noise types, even outperforming the supervised method, N2C. This is particularly evident in Poisson noise, where MeD surpasses N2C by ~**3 dB**. These results highlight the generalisation ability of our approach in handling unseen noise.

4.4. Experiments on General Noise Pool

Here we further investigate the generalisation ability of our method by introducing our general *Noise Pool*. The Noise Pool comprises the five aforementioned types of noise, each with a diverse range of noise levels. During training, we randomly sample from the noise pool to provide the model with noisy images. This novel approach simulates a realistic scenario where noise is unknown and can originate from various sources to some extent.

Specifically, we evaluated all methods using the random

noise pool approach to train and test on combined or single noise types. The results are summarised in Table 3.

Analysis: In Table 3, our MeD approach outperforms all other methods significantly on all the test noise types. For example, when a test noise containing a combination of Gaussian noise with $\hat{\sigma} = 50$ and Speckle noise with $\hat{v} = 25$ is used, other methods exhibit an approximate performance of ~27 dB. However, MeD achieves significantly better results with a performance of 29.68 dB. And on average, MeD exhibits a performance that is approximately 2 dB better than other methods. Our findings show that utilising a comprehensive noise pool for training purposes can effectively improve the generalisation capability. Furthermore, the remarkable denoising generalisation ability of our MeD approach, in comparison to other methods, is particularly advantageous for real-world applications.
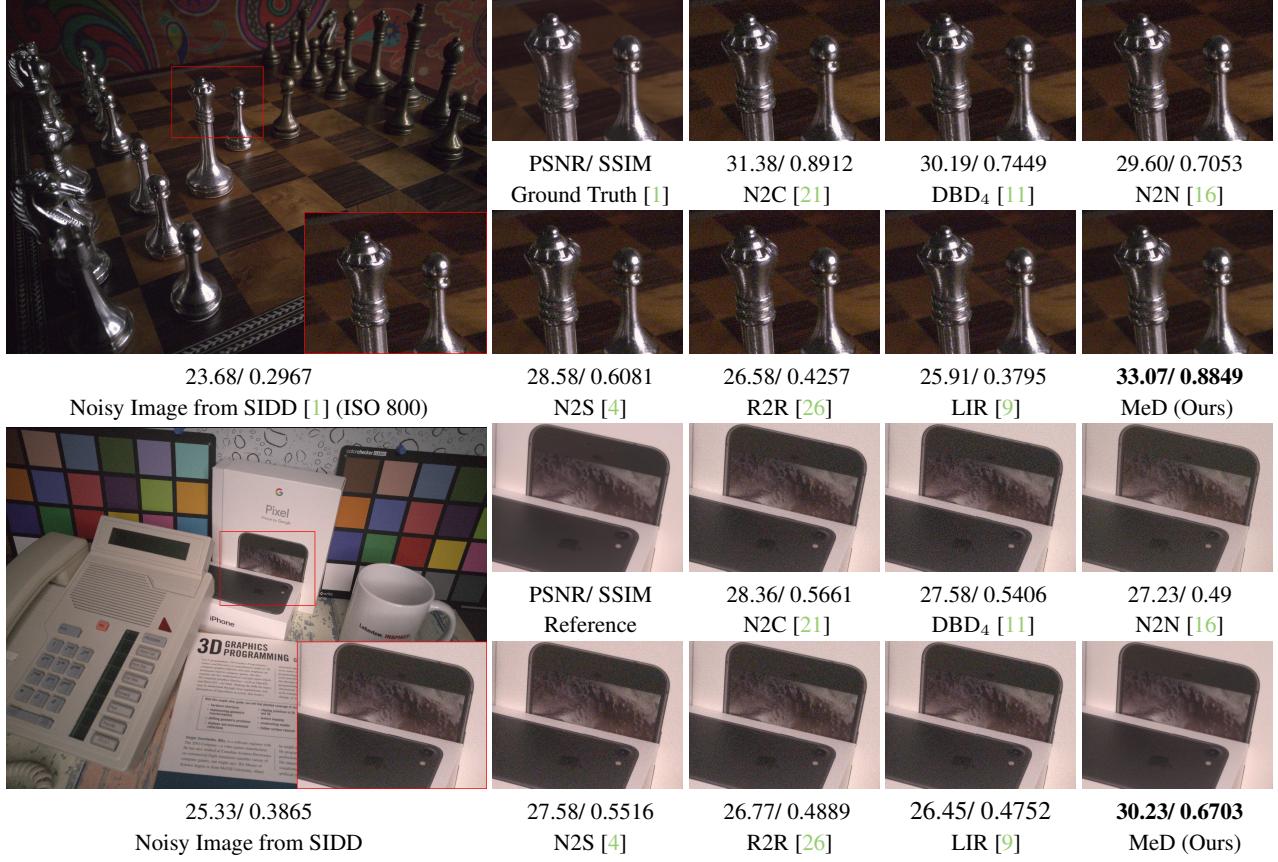
Figure 4. **Real Noise Removal Example of SIDD [1]**. All the methods are trained with *Noise Pool* on the DIV2K [2] dataset. It can be seen that the proposed MeD can remove much real noise even without training with real-noise distribution (zoom in for a better comparison).

Table 4. Quantitative result obtained from the application of various methods trained on a general Noise Pool to real noise datasets.

Method	PolyU [32]	SIDD [1]	CC [24]	Average
N2C [21]	35.89/ 0.9652	30.37/ 0.6028	37.89/ 0.9408	34.72/ 0.8363
DBD$_4$ [11]	35.69/ 0.9571	30.23/ 0.6173	37.74/ 0.9357	34.55/ 0.8367
N2N [16]	36.22/ 0.9679	32.82/ 0.7297	37.39/ 0.9570	35.48/ 0.8849
N2S [4]	36.41/ 0.9721	30.98/ 0.6018	37.58/ 0.9622	34.99/ 0.8454
R2R [26]	34.58/ 0.8890	29.64/ 0.5708	35.35/ 0.8478	33.19/ 0.7692
LIR [9]	34.81/ 0.7278	28.76/ 0.5296	35.50/ 0.8403	33.02/ 0.6992
MeD (ours)	**38.65/ 0.9855**	**35.81/ 0.8278**	**40.08/ 0.9745**	**38.18/ 0.9293**

4.5. Real Noise Removal

In our previous experiments, we demonstrated the exceptional denoising performance of our MeD approach on synthetic noises. However, real-world noise is often more complex and challenging than synthetic noise. In this subsection, we aim to evaluate the generalisation performance of our approach on real-world noise by testing it on the SIDD [1], CC [24] and PolyU [32] datasets. To assess the denoising performance on real-world noise, we use the same pre-trained models as in Section 4.4. The representative qualitative results on the SIDD dataset in the standard RGB colour space are presented in Figure 4.

Analysis: As shown in Table 4, our approach significantly outperforms all other methods across all three datasets, with a performance improvement of **2-3 dB** over the second-best approach, and also consistently outperforms its supervised counterparts (*i.e.* N2C and DBD$_4$) by over **3 dB**. These results suggest the effectiveness and generalisability of the proposed approach in real-world denoising scenarios.

Our approach achieves remarkable performance on real-world noise without even being trained on more expensive real-world data. For a more complete study, we also conduct experiments on model training with real-world data (for more details please refer to the supplementary material), showing superior performance and even better generalisation ability to data out of the training data distribution.

In Figure 4, the presence of noise persists even after applying denoising techniques, yet ours demonstrates the most authentic outcomes compared to others. For instance, while the noise particles remain prominent in the N2C results, they are absent in our results. Overall, the results indicate that the MeD approach is well-suited for real-world denoising tasks, providing a robust and reliable solution for

Table 5. Multiple views (≥ 2) study, with average PSNR/SSIM.

#Views	Gaussian	LVG	Poission	Speckle	S&P
2	29.61/ 0.8178	37.99/ 0.9568	48.10/ 0.9916	37.21/ 0.9715	42.33/ 0.9695
3	29.68/ 0.8197	38.05/ 0.9577	48.23/ 0.9920	37.40/ 0.9733	42.45/ 0.9703
4	29.70/ 0.8204	38.08/ 0.9580	48.31/ 0.9921	37.47/ 0.9740	42.49/ 0.9709

Table 6. Average PSNR/SSIM of super-resolution results on Set5 [6]. Learning-based methods are trained with *Corruption Pool*.

Scale	Bicubic	RCAN [37]	DASR [30]	MeD (ours)
×2	33.63/ 0.9285	36.12/ 0.9339	36.98/ 0.9471	**37.12/ 0.9527**
×3	30.37/ 0.8652	34.15/ 0.9286	34.11/ 0.9187	**34.92/ 0.9294**
×4	28.35/ 0.8084	31.94/ 0.8871	31.54/ 0.8736	**32.50/ 0.8956**

improving image quality in challenging environments.

4.6. Expand to More Views

Although we only showcase two views for the experiments above, our method can be easily expanded to multiple views. To investigate the impact of the numbers of views, here we further conduct a study comparing 2, 3, and 4 views, in Table 5.

The results indicate that increasing the number of views consistently improves the performance across different noise types. For example, when dealing with Speckle noise, the 4-view model achieves a 0.26 dB higher PSNR than the 2-view model. However, it is worth noting that employing n views requires $n!$ cross-computations within each view pair during training, resulting in a significant increase in computational cost (*e.g.* from 2-view to 4-view leads to a $10\times$ training time increase in our experiment).

4.7. More Application Exploration

Here we investigate the potential of the proposed MeD for other more general image restoration tasks, such as image super-resolution and inpainting. In this study, we generalise the previously defined *degradation (noise)* to a residual image between a clean image and a corrupted image. Moreover, we expand the definition from *Noise Pool* to a more general one – *Corruption Pool* that contains not only noise but also general corruption.

Super resolution. Image super-resolution aims to enlarge the resolution of a low-resolution image. We train our method on the DIV2K dataset [3], where we randomly choose different downscale methods from a *Corruption Pool* that consists of random Gaussian noise and four types of down-scaling (bicubic, lanczos, bilinear, and hamming). We benchmark our method against the supervised method RCAN [37] that aims for high PSNR and the recent unsupervised methods DASR [30] that are specialised for super-resolution. We conduct our evaluation on the Set5 dataset [6] with scaling factors of 2, 3, and 4. The results in Table 6 show the effectiveness of our method over both supervised and unsupervised approaches.

Table 7. Average PSNR/SSIM of inpainting results on Set11 [29]. S2S and DIP are trained and tested on the same single image. MeD is trained with *Corruption Pool*.

Dropping Ratio	DIP [29]	S2S [27]	MeD (Ours)
50%	33.45/ 0.9217	34.91/ 0.9479	**36.24/ 0.9617**
70%	28.53/ 0.8501	30.94/ 0.8845	**31.05/ 0.9161**
90%	24.39/ 0.7360	25.97/ 0.7933	**26.01/ 0.8052**

Inpainting. We also apply our method to the image inpainting task, which fills in missing pixels. We choose two single-image deep learning methods – Self2Self (S2S) [27] and DIP [29], for comparison. Our MeD is trained with *Corruption Pool* containing noises, down-scaling, and inpainting mask operations altogether. To compare our method (MeD) with other state-of-the-art methods, we conduct experiments on the Set 11 dataset [29] with three different pixel dropping ratios: 50%, 70%, and 90%. The results are shown in Table 7, suggesting the effectiveness of MeD again in the image inpainting task.

5. Conclusion

In this paper, we have presented a new self-supervised learning method (MeD) for image denoising that disentangles scene and noise features in a constraint feature space. Our approach has demonstrated exceptional denoising performance in both synthetic and real-world noise scenarios, with particularly significant performance on real-world noise. MeD can handle complex noise with better performance than other state-of-the-art methods, as validated by consistent performance gain across various datasets and noise types. Our approach has decent generalisation ability, requiring only noisy images for training and efficiently denoising real-world noise without seeing any clean ground truth data. This opens up new possibilities for training deep models without the need for costly labelled data. Furthermore, our model can be easily adapted to other low-level image restoration tasks. We hope this could provide a new baseline for future research in image disentanglement and the extension to other image processing tasks.

References

[1] Abdelrahman Abdelhamed, Stephen Lin, and Michael S Brown. A high-quality denoising dataset for smartphone cameras. In *Proceedings of the IEEE Conference on Computer Vision and Pattern Recognition*, pages 1692–1700, 2018.

[2] Eirikur Agustsson and Radu Timofte. Ntire 2017 challenge on single image super-resolution: Dataset and study. In *Proceedings of the IEEE conference on computer vision and pattern recognition workshops*, pages 126–135, 2017.

[3] Eirikur Agustsson and Radu Timofte. Ntire 2017 challenge on single image super-resolution: Dataset and study. In *The IEEE Conference on Computer Vision and Pattern Recognition (CVPR) Workshops*, July 2017.

[4] Joshua Batson and Loic Royer. Noise2self: Blind denoising by self-supervision. In *International Conference on Machine Learning*, pages 524–533. PMLR, 2019.

[5] Dominique Béréziat and Isabelle Herlin. Solving ill-posed image processing problems using data assimilation. *Numerical Algorithms*, 56(2):219–252, 2011.

[6] Marco Bevilacqua, Aline Roumy, Christine Guillemot, and Marie Line Alberi-Morel. Low-complexity single-image super-resolution based on nonnegative neighbor embedding. 2012.

[7] Chao Dong, Yubin Deng, Chen Change Loy, and Xiaoou Tang. Compression artifacts reduction by a deep convolutional network. In *Proceedings of the IEEE International Conference on Computer Vision*, pages 576–584, 2015.

[8] Chao Dong, Chen Change Loy, Kaiming He, and Xiaoou Tang. Learning a deep convolutional network for image super-resolution. In *European conference on computer vision*, pages 184–199. Springer, 2014.

[9] Wenchao Du, Hu Chen, and Hongyu Yang. Learning invariant representation for unsupervised image restoration. In *Proceedings of the IEEE/CVF conference on computer vision and pattern recognition*, pages 14483–14492, 2020.

[10] Rich Franzen. Kodak lossless true color image suite. *source: http://r0k. us/graphics/kodak*, 4(2), 1999.

[11] Clément Godard, Kevin Matzen, and Matt Uyttendaele. Deep burst denoising. In *Proceedings of the European conference on computer vision*, pages 538–554, 2018.

[12] Jun Guo and Hongyang Chao. Building dual-domain representations for compression artifacts reduction. In *European Conference on Computer Vision*, pages 628–644. Springer, 2016.

[13] Alexander Krull, Tim-Oliver Buchholz, and Florian Jug. Noise2void-learning denoising from single noisy images. In *Proceedings of the IEEE/CVF conference on computer vision and pattern recognition*, pages 2129–2137, 2019.

[14] Orest Kupyn, Tetiana Martyniuk, Junru Wu, and Zhangyang Wang. Deblurgan-v2: Deblurring (orders-of-magnitude) faster and better. In *Proceedings of the IEEE/CVF International Conference on Computer Vision*, pages 8878–8887, 2019.

[15] Samuli Laine, Tero Karras, Jaakko Lehtinen, and Timo Aila. High-quality self-supervised deep image denoising. In H. Wallach, H. Larochelle, A. Beygelzimer, F. d'Alché-Buc, E. Fox, and R. Garnett, editors, *Advances in Neural Information Processing Systems*, volume 32. Curran Associates, Inc., 2019.

[16] Jaakko Lehtinen, Jacob Munkberg, Jon Hasselgren, Samuli Laine, Tero Karras, Miika Aittala, and Timo Aila. Noise2noise: Learning image restoration without clean data. *arXiv preprint arXiv:1803.04189*, 2018.

[17] Jingyuan Li, Ning Wang, Lefei Zhang, Bo Du, and Dacheng Tao. Recurrent feature reasoning for image inpainting. In *Proceedings of the IEEE/CVF Conference on Computer Vision and Pattern Recognition*, pages 7760–7768, 2020.

[18] Jingyun Liang, Jiezhang Cao, Guolei Sun, Kai Zhang, Luc Van Gool, and Radu Timofte. Swinir: Image restoration using swin transformer. In *Proceedings of the IEEE/CVF International Conference on Computer Vision*, pages 1833–1844, 2021.

[19] Bee Lim, Sanghyun Son, Heewon Kim, Seungjun Nah, and Kyoung Mu Lee. Enhanced deep residual networks for single image super-resolution. In *Proceedings of the IEEE conference on computer vision and pattern recognition workshops*, pages 136–144, 2017.

[20] Yu-Lun Liu, Wei-Sheng Lai, Ming-Hsuan Yang, Yung-Yu Chuang, and Jia-Bin Huang. Learning to see through obstructions. In *Proceedings of the IEEE/CVF Conference on Computer Vision and Pattern Recognition*, pages 14215–14224, 2020.

[21] Ze Liu, Yutong Lin, Yue Cao, Han Hu, Yixuan Wei, Zheng Zhang, Stephen Lin, and Baining Guo. Swin transformer: Hierarchical vision transformer using shifted windows. In *Proceedings of the IEEE/CVF International Conference on Computer Vision*, 2021.

[22] Boyu Lu, Jun-Cheng Chen, and Rama Chellappa. Uid-gan: Unsupervised image deblurring via disentangled representations. *IEEE Transactions on Biometrics, Behavior, and Identity Science*, 2(1):26–39, 2019.

[23] David Martin, Charless Fowlkes, Doron Tal, and Jitendra Malik. A database of human segmented natural images and its application to evaluating segmentation algorithms and measuring ecological statistics. In *Proceedings of IEEE International Conference on Computer Vision*, volume 2, pages 416–423. IEEE, 2001.

[24] Seonghyeon Nam, Youngbae Hwang, Yasuyuki Matsushita, and Seon Joo Kim. A holistic approach to cross-channel image noise modeling and its application to image denoising. In *Proceedings of the IEEE conference on computer vision and pattern recognition*, pages 1683–1691, 2016.

[25] Reyhaneh Neshatavar, Mohsen Yavartanoo, Sanghyun Son, and Kyoung Mu Lee. Cvf-sid: Cyclic multi-variate function for self-supervised image denoising by disentangling noise from image. In *Proceedings of the IEEE/CVF Conference on Computer Vision and Pattern Recognition*, pages 17583–17591, 2022.

[26] Tongyao Pang, Huan Zheng, Yuhui Quan, and Hui Ji. Recorrupted-to-recorrupted: unsupervised deep learning for image denoising. In *Proceedings of the IEEE/CVF conference on computer vision and pattern recognition*, pages 2043–2052, 2021.

[27] Yuhui Quan, Mingqin Chen, Tongyao Pang, and Hui Ji. Self2self with dropout: Learning self-supervised denoising from single image. In *Proceedings of the IEEE/CVF conference on computer vision and pattern recognition*, pages 1890–1898, 2020.

[28] Marius Tico. Multi-frame image denoising and stabilization. In *European Signal Processing Conference*, pages 1–4. IEEE, 2008.

[29] Dmitry Ulyanov, Andrea Vedaldi, and Victor Lempitsky. Deep image prior. In *Proceedings of the IEEE/CVF conference on computer vision and pattern recognition*, pages 9446–9454, 2018.

[30] Longguang Wang, Yingqian Wang, Xiaoyu Dong, Qingyu Xu, Jungang Yang, Wei An, and Yulan Guo. Unsupervised degradation representation learning for blind super-resolution. In *Proceedings of the IEEE/CVF Conference on Computer Vision and Pattern Recognition*, pages 10581–10590, 2021.

[31] Zhangyang Wang, Ding Liu, Shiyu Chang, Qing Ling, Yingzhen Yang, and Thomas S Huang. D3: Deep dual-domain based fast restoration of jpeg-compressed images. In *Proceedings of the IEEE/CVF conference on computer vision and pattern recognition*, pages 2764–2772, 2016.

[32] Jun Xu, Hui Li, Zhetong Liang, David Zhang, and Lei Zhang. Real-world noisy image denoising: A new benchmark. *arXiv preprint arXiv:1804.02603*, 2018.

[33] Wentian Xu and Jianbo Jiao. Revisiting implicit neural representations in low-level vision. In *International Conference on Learning Representations Workshop*, 2023.

[34] Jiahui Yu, Zhe Lin, Jimei Yang, Xiaohui Shen, Xin Lu, and Thomas S Huang. Free-form image inpainting with gated convolution. In *Proceedings of the IEEE/CVF International Conference on Computer Vision*, pages 4471–4480, 2019.

[35] Kai Zhang, Wangmeng Zuo, Yunjin Chen, Deyu Meng, and Lei Zhang. Beyond a gaussian denoiser: Residual learning of deep cnn for image denoising. *IEEE transactions on image processing*, 26(7):3142–3155, 2017.

[36] Lei Zhang, Xiaolin Wu, Antoni Buades, and Xin Li. Color demosaicking by local directional interpolation and nonlocal adaptive thresholding. *Journal of Electronic imaging*, 20(2):023016, 2011.

[37] Yulun Zhang, Kunpeng Li, Kai Li, Lichen Wang, Bineng Zhong, and Yun Fu. Image super-resolution using very deep residual channel attention networks. In *Proceedings of the European conference on computer vision*, pages 286–301, 2018.

[38] Yuqian Zhou, Jianbo Jiao, Haibin Huang, Yang Wang, Jue Wang, Honghui Shi, and Thomas Huang. When awgn-based denoiser meets real noises. In *Proceedings of the AAAI Conference on Artificial Intelligence*, volume 34, pages 13074–13081, 2020.